

---

This manuscript is a non-peer reviewed EarthArXiv preprint submitted to  
Geophysical Research Letters.

---

# Antarctic Geothermal Heat Flow, Crustal Conductivity and Heat Production Inferred From Seismological Data

James A. N. Hazzard<sup>1</sup>, Fred D. Richards<sup>1</sup>

<sup>1</sup>Department of Earth Science & Engineering, Imperial College London, Royal School of Mines, Prince Consort Road, London, SW7 2AZ, UK

## Key Points:

- Demonstration of new methodology for inferring geothermal heat flow from seismological data.
- S- and P-wave velocity used together to infer and fit geotherms.
- Incorporation of laterally varying crustal conductivity and heat production.

## Abstract

Geothermal heat flow is a key parameter in governing ice dynamics, via its influence on basal melt and sliding, englacial rheology, and erosion. It is expected to exhibit significant lateral variability across Antarctica. Despite this, surface heat flow derived from Earth's interior remains one of the most poorly constrained parameters controlling ice-sheet evolution. To obtain a continent-wide map of Antarctic heat supply at regional-scale resolution, we estimate upper mantle thermomechanical structure directly from  $V_S$ . Until now, direct inferences of Antarctic heat supply have assumed constant crustal composition. Here, we explore a range of crustal conductivity and radiogenic heat production values by fitting thermodynamically self-consistent geotherms to their seismically inferred counterparts. Independent estimates of crustal conductivity derived from  $V_P$  are integrated to break an observed trade-off between crustal parameters, allowing us to infer Antarctic geothermal heat flow and its associated uncertainty.

## Plain Language Summary

The future evolution of the Antarctic Ice Sheet depends on its stability, which describes how sensitive it is to environmental change. A key factor influencing ice sheet stability is how much thermal energy is transferred into its base from Earth's interior: a parameter called geothermal heat flow. If the level of heat supply is high, melting at the base of the ice sheet is encouraged, resulting in enhanced sliding towards outlet glaciers at the continental perimeter. Consequently, ice loss is accelerated, and the likelihood of glacial collapse is increased. Therefore, an accurate map of Antarctic geothermal heat flow, including how this parameter varies from region to region, is needed to produce high quality projections of Antarctic ice mass loss and therefore global sea level change. In this study, we use models of how seismic wave speed varies within Earth to estimate its three-dimensional temperature structure, as well as its thermal conductivity. These data are used to infer a collection of best-fitting models of Earth's thermal state, and hence estimate Antarctic geothermal heat flow.

---

Corresponding author: James A. N. Hazzard, [j.hazzard20@imperial.ac.uk](mailto:j.hazzard20@imperial.ac.uk)

## 1 Introduction

Heat derived from Earth’s interior, and supplied to its surface, is a crucial component of ice sheet basal conditions. The supply of thermal energy to the ice sheet-solid Earth interface can influence basal melt and sliding, englacial rheology, and erosion, and is therefore a key factor in governing ice dynamics (Larour et al., 2012; Burton-Johnson et al., 2020). Not only are ice dynamics highly sensitive to the supply of geothermal heat, the latter is expected to vary significantly across Antarctica (e.g., Shen et al., 2020). The result is that a good understanding of the pattern and amplitude of heat supply into the base of the Antarctic Ice Sheet is a requirement for accurately modelling its evolution.

To quantify heat supply we refer to geothermal heat flow (GHF),  $q_s$ , pertaining to the amount of thermal energy supplied across Earth’s surface, per unit area and time (units  $\text{mW m}^{-2}$ ). Since thermal conduction is the dominant mechanism of heat transfer in Earth’s crust, Fourier’s law of conduction is used to relate  $q_s$  to Earth’s temperature structure,

$$\vec{\mathbf{q}}_s = -k(z = z_0) \frac{\partial T}{\partial z} \Big|_{z=z_0} \hat{\mathbf{z}}, \quad (1)$$

$$q_s = |\vec{\mathbf{q}}_s|. \quad (2)$$

Here,  $k$  is thermal conductivity,  $T$  is temperature,  $z$  is a locally vertical depth co-ordinate, and  $z_0$  is located at the surface. Theoretically, then, Equation 1 gives us a pathway to estimating  $q_s$ , via measurements of laterally varying thermomechanical structure. Indeed, local estimates of Antarctic GHF have been made using observations of temperature and depth from boreholes into unconsolidated sediment, ice, or bedrock. However, such measurements can only be used to infer point estimates of GHF.

To obtain continental scale maps of GHF in Antarctica suitable for ice sheet modelling, geophysical methods are an extremely valuable tool. A number of methods based on magnetic, gravity or seismic data have been employed in the past (e.g., An et al., 2015; Martos et al., 2017; Haeger et al., 2022). Whilst useful, such methods have suffered from a range of data- and modelling-derived issues. For example, sparsity of data and a lack of sensitivity to short-wavelength structure has led to poor spatial resolution of inferred GHF models. Poor constraint on crustal parameters such as thermal conductivity and heat production has led to lateral variations being ignored, despite their potential to vary significantly, and the consequent impact of such variations on GHF. Difficulties in converting field observations into estimates of Earth’s thermal structure, and the inference of only a single isotherm, has led to large uncertainty in GHF predictions.

A number of recent advances allow for the establishment of a novel approach to infer GHF from seismological data sets. Firstly, the development of ANT-20, a wave-equation traveltime adjoint tomographic model, lays the groundwork for imaging Antarctic thermomechanical structure and henceforth GHF at regional-scale resolution ( $\sim 100$  km) (Lloyd et al., 2020; Hazzard et al., 2023). Secondly, new geochemical analyses have improved our understanding of the likely range of key crustal parameters governing heat supply, their relationship with composition, and to what extent they can be inferred from geophysical data (Sammon et al., 2022; Jennings et al., 2019). Thirdly, the emergence of physics-based parameterisations of mantle rock properties, constrained via laboratory experiments, has opened the door to converting seismic velocities directly into temperature (Faul & Jackson, 2005; Yamauchi & Takei, 2016; Yabe & Hiraga, 2020). In addition, methods to calibrate these parameterisations based on a range of geophysical data constraints have allowed us to reduce uncertainty in such conversions (Richards et al., 2020; Hazzard et al., 2023).

Here, we harness the aforementioned advances to produce a new model of Antarctic GHF and its associated uncertainty, based on a new approach integrating both shear- ( $V_S$ ) and compressional- ( $V_P$ ) wave velocity data. In Section 2, the methodological details underpinning this approach are described, including details of how the data are utilised

85 to co-constrain crustal conductivity, heat production, and surface GHF. In Section 3, we  
 86 present our model of seismically inferred GHF, and interpret our results within the con-  
 87 text of previous geophysical studies.

## 88 2 Methods

89 Our approach to inferring GHF across Antarctica is motivated by the desire to in-  
 90 fer geothermal structure in as direct a fashion as possible, without relying on empirical  
 91 comparisons to measured GHF in geologically distinct continental environments. Cen-  
 92 tral to this approach is the idea of constraining the relationship between temperature  
 93 and depth,  $T(z)$ , across a range of depth slices, rather than relying on a single isotherm.  
 94 Therefore, we make use of  $V_S$  data, which is especially sensitive to geothermal structure  
 95 throughout the shallow upper mantle. Since crustal composition also plays a key role in  
 96 determining heat supply, via variations in thermal conductivity and heat production, we  
 97 seek to constrain these parameters within our modelling framework. To do so, we bring  
 98 in information from  $V_P$  data, which provides sensitivity to lateral variations in  $\text{SiO}_2\%$   
 99 content and therefore crustal conductivity. By fitting steady-state geothermal profiles  
 100 to  $V_S$ -derived counterparts, and looking at how the misfit between the two varies as a  
 101 function of crustal heat production, we are able to co-constrain conductivity, heat pro-  
 102 duction and geothermal heat flow in a thermodynamically self-consistent fashion. This  
 103 framework serves as the basis for providing reasonable inferences of  $q_s$ .

### 104 2.1 Inferring Thermal Structure from Seismic Data

105 The sensitivity of  $V_S$  to temperature ( $T$ ) derives from the effect that temperature  
 106 has on the viscoelastic properties of mantle rock. To reliably parameterise the  $V_S(T)$   
 107 relationship, we adopt the approach of [Hazzard et al. \(2023\)](#), who calibrated the anelas-  
 108 ticity parameterisation of [Yamauchi & Takei \(2016\)](#) against a suite of Antarctic geophys-  
 109 ical data constraints (see Section S1 for details). Having established a method for relat-  
 110 ing seismic velocity and temperature, we can select a geographic location  $\{\theta, \phi\}$  (longi-  
 111 tude,  $\theta$ , latitude,  $\phi$ ) within the spatial footprint of the chosen tomographic model ANT-  
 112 20, and convert the corresponding radial velocity structure  $V_S(z)$  into an inferred geotherm  
 113  $T(z)$  (Figure 1a, black cross-hairs).

### 114 2.2 Fitting Geothermal Profiles

115 Due to the likely presence of noise and artefacts in the underlying seismic data, as  
 116 well as the potential for unmodelled compositional seismic velocity variation, we avoid  
 117 estimating  $q_s$  directly from our seismically inferred geotherms. Instead, we fit steady-  
 118 state, thermodynamically self-consistent geotherms to them. To prepare the  $V_S$ -derived  
 119 geotherms for fitting, we clean and interpolate them on a 1 km interval (see Section S1  
 120 for details, Figure 1a, red dashed line).

121 We fit the geotherms according to a modified version of the procedure laid out in  
 122 [McKenzie et al. \(2005\)](#). This procedure involves iteratively updating the Moho GHF,  
 123 and mechanical boundary layer thickness, until the misfit between modelled and  $V_S$ -derived  
 124 geotherms is minimised. Once an optimal geotherm has been arrived at (Figure 1a, black  
 125 solid line),  $q_s$  can be calculated according to the surface temperature gradient and as-  
 126 sociated thermal conductivity.

### 127 2.3 Parameterising Mantle Structure

128 In addition to providing a seismically inferred geotherm to the fitting procedure,  
 129 we must also provide a suitable parameterisation for thermal conductivity,  $k$  ( $\text{W m}^{-1} \text{K}^{-1}$ ),  
 130 and heat production,  $h^*$  ( $\mu\text{W m}^{-3}$ ), in the mantle and crust.

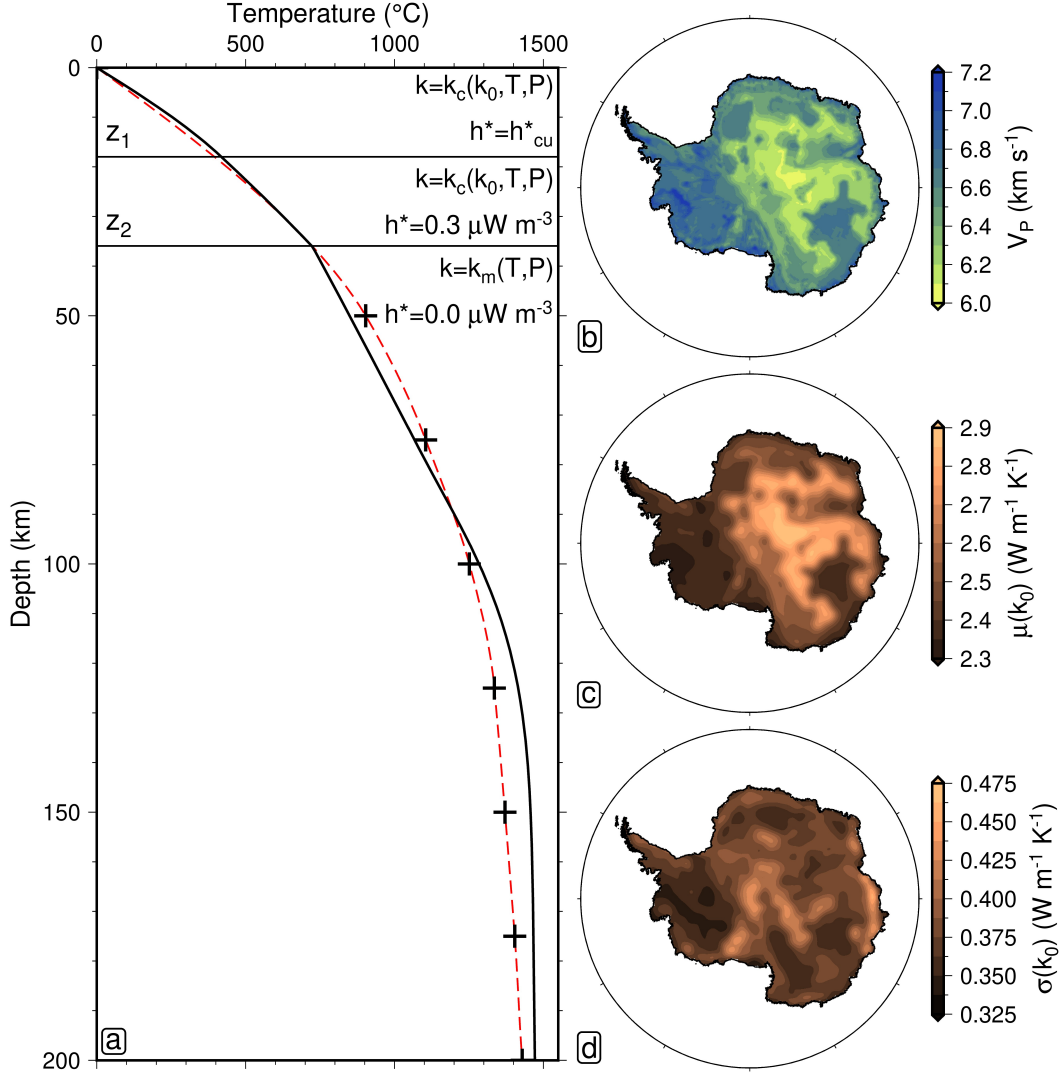


**Figure 1. Parameterising Earth structure.** (a) Temperature-depth data points inferred from  $V_S$  (black cross-hairs) interpolated prior to fitting (red dashed line). Steady-state geotherm fitted to seismic data (black line), subject to depth-dependent thermodynamic constraints within the upper crust ( $0 \leq z \leq z_1$ ), lower crust ( $z_1 < z \leq z_2$ ), and mantle ( $z_2 < z$ ). All depths referenced with respect to the crystalline basement. (b) Average crustal  $V_P$  across Antarctica. (c) Crustal conductivity ( $k_0$ ) estimated from  $V_P$  (Equation 4). (d) Uncertainty in  $k_0$  based on spread in crustal  $V_P$  and  $k_0(V_P)$  residual (Section 2.5).

131 In the mantle, we calculate conductivity according to the temperature- and pressure-  
 132 dependent parameterisation of [Korenaga & Korenaga \(2016\)](#). We have adapted this pa-  
 133 rameterisation to assume a grain size of 0.1 cm, relevant to the calculation of radiative  
 134 thermal conductivity. We refer to this parameterisation as  $k = k_m(T, P)$ . In accordance  
 135 with the relatively low-abundance of heat-producing elements in the upper mantle, we  
 136 assume a mantle heat production  $h^* = 0.0 \mu\text{W m}^{-3}$ . We set constant-pressure heat ca-  
 137 pacity to  $C_P = 1187 \text{ J kg}^{-1} \text{ K}^{-1}$ , and thermal expansivity to  $\alpha = 3 \times 10^{-5} \text{ K}^{-1}$ , in  
 138 our assumptions of adiabatic mantle properties. We assume a mantle kinematic viscos-  
 139 ity of  $\nu = 9 \times 10^{16} \text{ m}^2 \text{ s}^{-1}$ .

## 140 2.4 Parameterising Crustal Structure

141 To parameterise thermal conductivity in the crust, we make use of the following  
 142 parameterisation ([Goes et al., 2020](#)), which we refer to as  $k = k_c(k_0, T, P)$ ,

$$143 \quad k_c(k_0, T, P) = \frac{k_0}{n} (1 + \beta P) \left( n - 1 + \exp \left[ \frac{-(T - 25)}{300} \right] \right). \quad (3)$$

144 In this equation, the factors  $\beta = 0.1$ , and  $n = 6.4 - 2.3 \ln(k_0)$ , and  $k_0$  is the ref-  
 145 erence crustal conductivity at atmospheric conditions ( $P = 0 \text{ GPa}$ ,  $T = 25^\circ\text{C}$ ). Note  
 146 that this parameterisation was misprinted in the original text of [Goes et al. \(2020\)](#); we  
 147 have clarified with the authors that the expression above is the correct version.

148 To parameterise heat production, we divide the crust into two layers of equal depth.  
 149 We assume a uniformly distributed heat production throughout each layer, set to  $h^* =$   
 150  $h_{\text{cu}}^*$  in the upper crust, and  $h^* = 0.3 \mu\text{W m}^{-3}$  in the lower crust. We have adopted this  
 151 simple parameterisation to avoid imposing precise details of the depth-dependence of  $h^*$   
 152 *a priori*, which are not known. When the upper crustal heat production is set to  $h_{\text{cu}}^* = 1.0 \mu\text{W m}^{-3}$ ,  
 153 our parameterisation is consistent with globally averaged heat production values obtained  
 154 from a comprehensive analysis of crustal geochemistry and seismic velocity ([Sammon et](#)  
 155 [al., 2022](#)).

## 156 2.5 Sampling Crustal Parameters to Optimise GHF

157 Reference thermal conductivity,  $k_0$ , and upper crustal heat production,  $h_{\text{cu}}^*$ , are treated  
 158 as laterally variable parameters in our model, so as to account for the influence of crustal  
 159 composition on geothermal structure. Both parameters could exhibit lateral variability  
 160 within the approximate ranges  $k_0 \sim 1.0$  to  $4.0 \text{ W m}^{-1} \text{ K}^{-1}$  and  $h_{\text{cu}}^* \sim 0.0$  to  $6.0 \mu\text{W m}^{-3}$   
 161 ([Hasterok & Chapman, 2011](#); [Jennings et al., 2019](#); [Lösing et al., 2020](#); [Sammon et al.,](#)  
 162 [2022](#)). Such variations can have a significant impact on  $q_s$ . For example, we found that  
 163 for a typical  $V_S$ -derived input geotherm, varying  $k_0$  and  $h_{\text{cu}}^*$  within the aforementioned  
 164 ranges results in surface GHF variations of  $q_s \sim 20$  to  $170 \text{ mW m}^{-2}$ . The lowest (high-  
 165 est) inferred  $q_s$  occurs when both  $k_0$  and  $h_{\text{cu}}^*$  are minimised (maximised). We can ratio-  
 166 nalise this observation by considering the dependence of  $q_s$  on each crustal parameter  
 167 in turn (see Section S2 for details).

168 In order to optimise our predictions of GHF at each location, we co-vary  $k_0$  and  
 169  $h_{\text{cu}}^*$ , and evaluate the least-squared misfit between  $V_S$ -inferred and fitted geotherms as  
 170 a function of the two free parameters (Figure 2). If the misfit space at each location were  
 171 to exhibit a global minimum, this would allow for simultaneous extraction of best-fitting  
 172  $k_0$ ,  $h_{\text{cu}}^*$  and  $q_s$ . However, we find that  $k_0$  and  $h_{\text{cu}}^*$  trade off significantly with one another.  
 173 This trade-off can be visualised by holding  $k_0$  constant and varying  $h_{\text{cu}}^*$ , and vice versa,  
 174 and observing the similarity in fitted geotherms (Figure 2, panels a-b). Of course, this  
 175 similarity is also borne out in the misfit space, where we see valley-like minima (Figure  
 176 2c). Since  $q_s$  trades-off positively with both  $k_0$  and  $h_{\text{cu}}^*$ , it is vital to be able to locate  
 177 where in the valley of the misfit space the so-called true solution lies. To resolve this is-

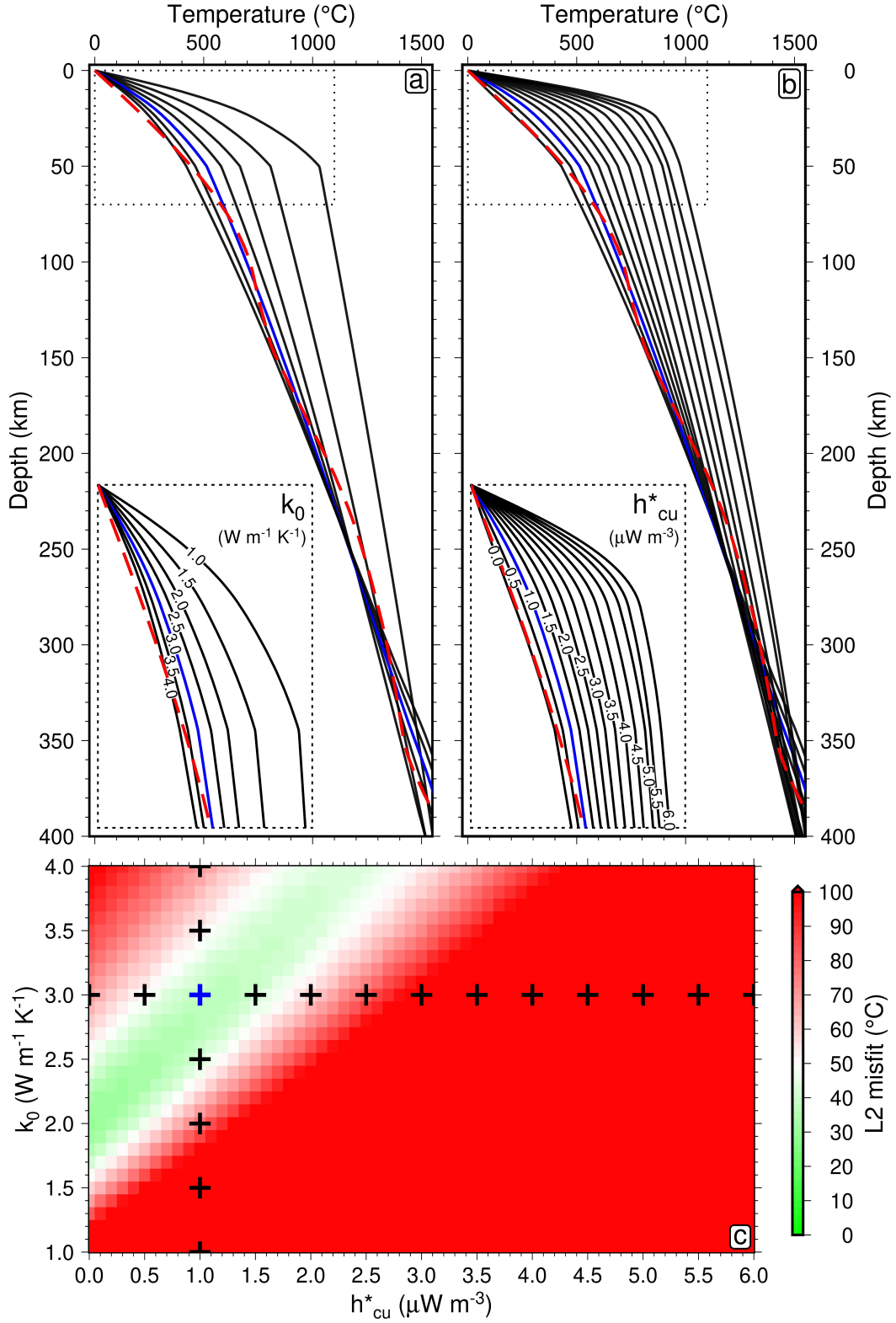


**Figure 2. Fitting seismically inferred geotherms.** (a) Constant reference conductivity,  $k_0 = 2.5 \text{ W m}^{-1} \text{ K}^{-1}$ , variable upper crustal heat production,  $h_{cu}^*$  in range 0.0 to  $6.0 \mu\text{W m}^{-3}$ . (b) Variable reference conductivity,  $k_0$  in range 1.0 to  $4.0 \text{ W m}^{-1} \text{ K}^{-1}$ , constant upper crustal heat production,  $h_{cu}^* = 0.5 \mu\text{W m}^{-3}$ . (c) Trade-off between crustal conductivity and upper crustal heat production in misfit between seismically inferred and steady-state fitted geotherm ( $k_0$  and  $h_{cu}^*$  combinations used in panels (a) and (b) marked by cross-hairs).

178 sue and break the observed trade-off, we require additional information, which we ob-  
 179 tain by utilising an independent geophysical constraint on  $k_0$ .

180 To gain insight into laterally varying crustal conductivity, we draw on a model of  
 181 crustal  $V_P$  ( $\text{km s}^{-1}$ , Figure 1b). We use the same  $V_P$  model as was assumed in ANT-20,  
 182 for consistency with our chosen crustal thickness model. Jennings et al. (2019) relate  $V_P$   
 183 to  $k_0$  via laboratory measurements on igneous rocks spanning a wide range of compo-  
 184 sitions. They found that  $\text{SiO}_2$  is the dominant control on thermal conductivity. By mak-  
 185 ing use of the empirical relationship,

$$\begin{aligned}
 186 \quad k_0(V_P) &= a_0 + a_1 V_P + a_2 V_P^2, & (4) \\
 187 \quad a_0 &= 3.162 \times 10^1 \text{ W m}^{-1} \text{ K}^{-1}, \\
 188 \quad a_1 &= -8.263 \times 10^{-3} \text{ W m}^{-2} \text{ K}^{-1} \text{ s}^{-1}, \\
 189 \quad a_2 &= 5.822 \times 10^{-7} \text{ W m}^{-3} \text{ K}^{-1} \text{ s}^{-2}, \\
 190 \\
 191 \\
 192
 \end{aligned}$$

193 as provided by Jennings et al. (2019), we estimate Antarctic crustal conductivity by av-  
 194 eraging crustal  $V_P$  (in  $\text{km s}^{-1}$ ) at each continental location, and converting it into  $k_0$  (Fig-  
 195 ure 1c). In addition, we utilise the spread in  $V_P$  data within the crust at each location,  
 196 along with the  $k_0(V_P)$  fitting residual of  $0.31 \text{ W m}^{-1} \text{ K}^{-1}$ , to estimate an uncertainty in  
 197 our predicted conductivity (Figure 1d).

198 Since we now have access to independent predictions of  $k_0(\theta, \phi)$  derived from  $V_P$   
 199 data, we can locate physically plausible regions of  $k_0$ -space. We start by sampling a value  
 200 of  $k_0$  from a Gaussian distribution at each location, according to

$$201 \quad k_0 \sim \mathcal{N}[\mu(k_0), \sigma(k_0)], \quad (5)$$

202 where  $\mu(k_0)$  is given by the empirical prediction of equation 9, and  $\sigma(k_0)$  is given by the  
 203 uncertainty associated with this prediction (Figure 1). For each sampled value of  $k_0$ , we  
 204 extract the corresponding best fitting value of  $h_{\text{cu}}^*$ , as well as the  $q_s$  associated with this  
 205 combination of crustal parameters. By repeating this sampling procedure, we build up  
 206 a distribution of  $k_0$ ,  $h_{\text{cu}}^*$  and  $q_s$ . We summarise these distributions at each location us-  
 207 ing a mean and standard deviation, providing us with Antarctic GHF predictions along  
 208 with an estimate of their uncertainty.

### 209 3 Results and Discussion

#### 210 3.1 Antarctic GHF Estimates

211 Resulting estimates of Antarctic GHF are shown in Figure 3. To distinguish be-  
 212 tween West and East Antarctica, we utilise the satellite-mapped drainage network of Zwally  
 213 & Giovinetto (2011). Our results indicate high  $q_s$  in West Antarctica, where heat sup-  
 214 ply into the base of the Antarctic Ice Sheet is estimated to vary between  $60$  and  $130 \text{ mW m}^{-2}$ ,  
 215 and is on average  $97 \pm 14 \text{ mW m}^{-2}$  (median, and median absolute deviation, respectively).  
 216 Such GHF values are significantly higher than the global continental average,  $q_s = 67 \pm$   
 217  $47 \text{ mW m}^{-2}$  (as inferred from borehole temperature-depth data), and are in fact inter-  
 218 mediate between the former and the global average over continental rift zones,  $q_s = 114 \pm$   
 219  $94 \text{ mW m}^{-2}$  (Lucazeau, 2019). This result is consistent with recent tectonic activity, ev-  
 220 idence for Cenozoic magmatism, and inferences of a thermal anomaly beneath West Antarc-  
 221 tica (Ball et al., 2021; Hazzard et al., 2023; Barletta et al., 2018). The distribution of  
 222  $q_s$  values within the aforementioned range is relatively uniform, implying significant lat-  
 223 eral heterogeneity across West Antarctica. Maximum  $q_s$  is inferred at the continental  
 224 perimeter in the Amundsen Sea region, and in the northern Antarctic Peninsula.

225 In East Antarctica, our results indicate  $q_s$  in the range  $20$  to  $120 \text{ mW m}^{-2}$ . Note  
 226 that the presence of above-continental-average GHF values within this range is indica-  
 227 tive of the fact that not all of our defined East Antarctic region is underlain by cold, cra-  
 228 tonic material. However, the distribution of inferred GHF is heavily skewed towards lower



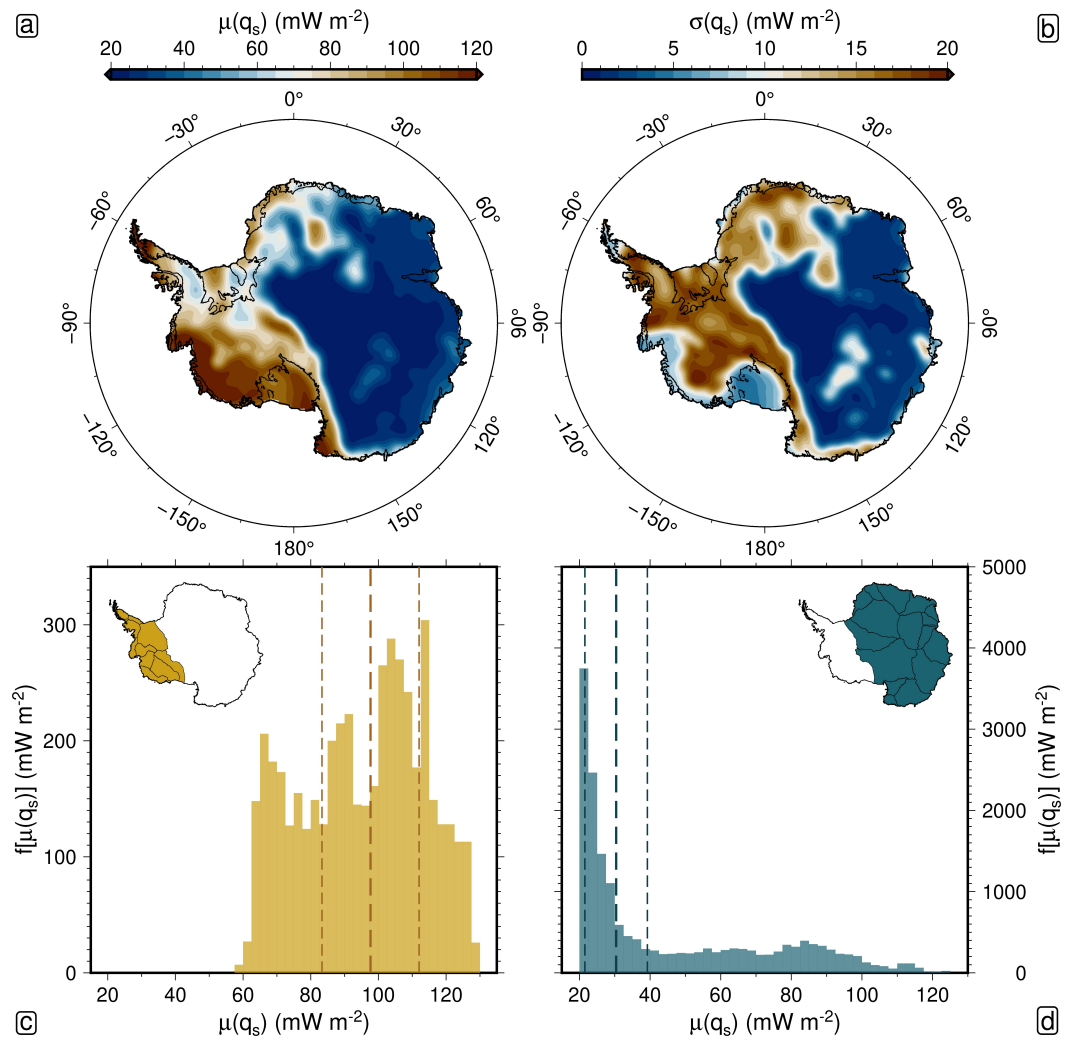


**Figure 3. Seismically inferred GHF.** (a) Mean. (b) Standard deviation. (c) Distribution over West Antarctica (region defined according to satellite-mapped drainage networks of [Zwally & Giovinetto, 2011](#)). (d) Same as (c), East Antarctica.

229 values, which is borne out in the spatial average  $30 \pm 8 \text{ mW m}^{-2}$ . Such low values are  
 230 consistent with globally averaged GHF estimates in continental regions of Archean age,  
 231  $q_s = 46 \pm 21 \text{ mW m}^{-2}$  (Lucazeau, 2019).

232 For the most part, the spatial pattern of GHF uncertainty,  $\sigma(q_s)$ , is similar to that  
 233 of the GHF prediction itself,  $\mu(q_s)$ . The ratio of these two predictions,  $\sigma(q_s)/\mu(q_s)$ , is  
 234 on average  $16 \pm 10\%$  over the Antarctic continent. Elevated proportional uncertainty  
 235 in GHF structure is estimated in Coats Land and Dronning Maud Land in East Antarc-  
 236 tica, in parallel with anomalously high uncertainty in heat production. The least-squared  
 237 misfit between inferred and modelled geotherm is relatively insensitive to the choice of  
 238 heat production here, reducing our ability to constrain this parameter and hence  $q_s$ . Anoma-  
 239 lously low  $q_s$  uncertainty ( $\sigma(q_s) < 10 \text{ mW m}^{-2}$ ) is estimated at the Amundsen Sea Em-  
 240 bayment and Ross Ice Shelf, as well as along the grounding line between these two re-  
 241 gions. These areas are characterised by high inferred GHF in the region of 100 to  $130 \text{ mW m}^{-2}$ .  
 242 The uncertainty here is artificially low owing to the inferred heat production lying at the  
 243 top of the parameter sweep range,  $h_{\text{cu}}^* = 6.0 \mu\text{W m}^{-3}$  (see Section S3 for maps of inferred  
 244  $h_{\text{cu}}^*$ ). Since the seismically inferred geotherm here is systematically hotter than the mod-  
 245 elled profile, the inferred value of  $h_{\text{cu}}^*$  is insensitive to variations in crustal thermal con-  
 246 ductivity, and thus exhibits no variation. We refrain from increasing the upper limit of  
 247 our parameter sweep in response to this issue, as this would not be an appropriate res-  
 248 olution, since  $h_{\text{cu}}^*$  values in excess of  $6.0 \mu\text{W m}^{-3}$  are inconsistent with the range of phys-  
 249 ically plausible values based on continental geology (Artemieva et al., 2017; Sammon et  
 250 al., 2022), and unreasonable increases in  $h_{\text{cu}}^*$  would be required to attempt to fit the in-  
 251 ferred geotherm. Instead, we suggest that the reason for our findings is due to our as-  
 252 sumption of a steady-state geotherm. While this assumption is a reasonable approxima-  
 253 tion across most of Antarctica, it may be less accurate in regions recently affected by in-  
 254 traplate basaltic magmatism and/or episodes of rifting (e.g., Alexander Island offshore  
 255 Antarctic Peninsula, Marie Byrd Land and the Victoria Land Basin; LeMasurier, 2008;  
 256 Sauli et al., 2021). Indeed, by locally modelling time-dependent thermal evolution fol-  
 257 lowing lithospheric thinning, we improve fit to  $V_S$ -derived temperature in these regions  
 258 and find that optimal transient geotherms require less extreme  $h_{\text{cu}}^*$  values than steady-  
 259 state equivalents (see Section S4 for transient geotherm modelling). Nevertheless, pre-  
 260 dicted  $q_s$  is near-identical for the these two different model assumptions, indicating that,  
 261 while our steady-state-based prediction likely overestimates  $h_{\text{cu}}^*$ , our  $q_s$  estimates remain  
 262 valid. Note, however, that uncertainty on  $q_s$  is likely higher than predicted in these lo-  
 263 cations, since the low uncertainty is likely an artefact of the  $6.0 \mu\text{W m}^{-3}$  upper limit we  
 264 impose on upper crustal heat production.

### 265 3.2 Comparison with previous studies

266 A comparison of our GHF model with those from previous studies utilising a range  
 267 of approaches is presented in Figure 4. Consistent across all studies, we observe a long-  
 268 wavelength pattern of elevated heat supply in West Antarctica, and more uniformly low  
 269 heat supply in East Antarctica. However, short-wavelength ( $\sim 1,000\text{--}10,000 \text{ km}$ ) struc-  
 270 ture differs significantly between models (both in terms of spatial pattern, and ampli-  
 271 tude), reflecting the range of data sets and modelling assumptions used to construct them.  
 272 In particular, our model (H23v2, Figure 4) spans a significantly greater range ( $110 \text{ mW m}^{-2}$ )  
 273 than any other, with the exception of Martos et al. (2017). The higher amplitude of GHF  
 274 variations in this study as compared to other models can be explained by our incorpo-  
 275 ration of laterally heterogeneous crustal composition. In East Antarctica we infer be-  
 276 low average crustal heat production, and in West Antarctica we see the opposite; the com-  
 277 bined effect of which is to broaden the range of inferred  $q_s$ . As compared to a directly  
 278 analogous model assuming constant  $k_0 = 2.5 \text{ W m}^{-1} \text{ K}^{-1}$  and  $h_{\text{cu}}^* = 1.0 \mu\text{W m}^{-3}$ , we  
 279 predict a 30% increase in maximum Antarctic  $q_s$ , and a 50% reduction in minimum Antarc-  
 280 tic  $q_s$  (Hazzard et al., 2023).

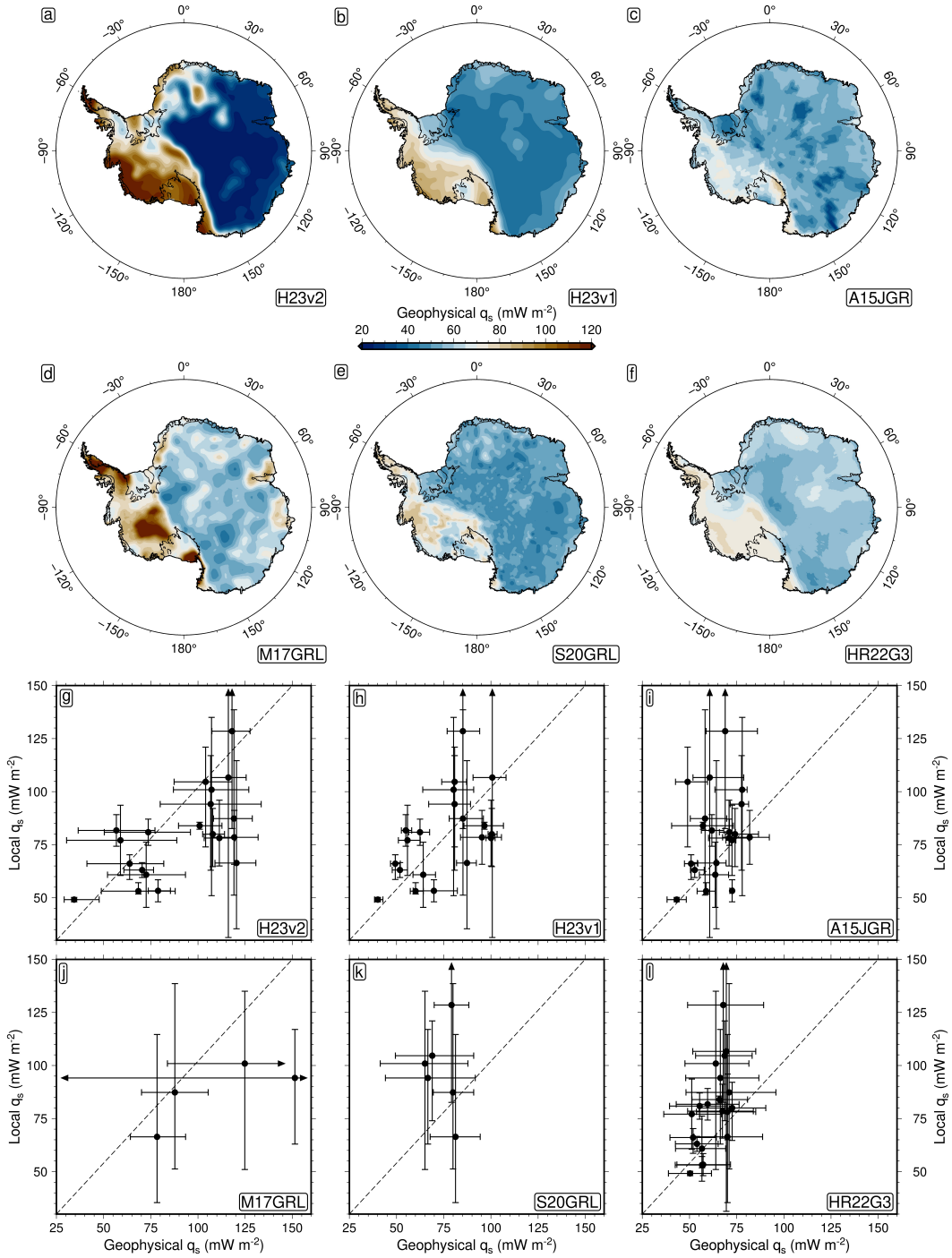


**Figure 4. GHF Model Comparison.** (a)–(f) Geophysical  $q_s$  inferences: H23v2 – inferred directly from  $V_S$  and  $V_P$  (this study); H23v1 – inferred directly from  $V_S$  (Hazzard et al., 2023); A15JGR – inferred directly from  $V_S$  (An et al., 2015); M17GRL – inferred from magnetic anomaly data (Martos et al., 2017); S20GRL – inferred empirically via  $V_S$  (Shen et al., 2020); HR22G3 – inferred via joint seismic and gravity inversion (Haeger et al., 2022). (g)–(l) Relationship between geophysically and locally inferred  $q_s$  (Section 3.3), same studies as (a)–(f).

### 281 3.3 Comparison with local data

282 Despite the sparsity of Antarctic GHF estimates derived from borehole measure-  
 283 ments of temperature and depth, these data can be utilised to independently assess geo-  
 284 physically informed models of  $q_s$ . It is important to treat borehole inferences carefully,  
 285 since they are representative of localised temperature structure, and are potentially sus-  
 286 ceptible to contamination by thermal signals caused by frictional heating at the base of  
 287 the ice sheet, and hydrological circulation (Shen et al., 2020). In addition, limited lat-  
 288 eral resolution in our chosen  $V_S$  model will smooth out GHF variations on spatial scales  
 289 smaller than  $\sim 100$  km, diminishing our ability to accurately compare to local estimates.  
 290 Therefore, we collect local estimates of  $q_s$  into regions of dimension 100 km, and com-  
 291 pare the average locally and geophysically inferred GHF values in each region. Perform-  
 292 ing such a comparison using each of the models shown in Figure 4, we find that the range  
 293 of GHF values predicted by our model is in better agreement with the local data than  
 294 those of any other study.

### 295 3.4 Methodological Appraisal

296 There are a few reasons why our modelling approach may allow us to arrive at es-  
 297 timates of GHF more consistent with independent data than previous studies. Firstly,  
 298 the use of a geophysically constrained parameterisation of mantle viscoelasticity enables  
 299 us to map  $V_S$  structure directly into temperature over a range of upper mantle depth  
 300 slices. This stands in contrast to other studies, such as those based on magnetic data,  
 301 where only a single isotherm associated with the Curie depth is constrained (Martos et  
 302 al., 2017). As a result, more reliable estimates of the geothermal gradient can be made.  
 303 Secondly, the incorporation of crustal  $V_P$  information provides us with sensitivity to lat-  
 304 eral variations in thermal conductivity, a parameter which affects  $q_s$  both directly via  
 305 its presence in Equation 1, and to a lesser extent, indirectly via its effect on the geother-  
 306 mal gradient. Thirdly, by combining insights drawn from  $V_S$  and  $V_P$  data together with  
 307 thermodynamic models of geothermal structure, we are able to constrain variations in  
 308 crustal heat production. This stands in contrast to previous studies making use of steady-  
 309 state geotherm modelling, which have assumed constant composition (An et al., 2015;  
 310 Haeger et al., 2022; Hazzard et al., 2023). In addition, methods based on empirical com-  
 311 parison of seismic data between continents are unable to account for differences in crustal  
 312 composition between target and comparison sites (Shen et al., 2020). Therefore, whilst  
 313 their inferred  $q_s$  uncertainty may implicitly capture variations in heat supply associated  
 314 with crustal composition, their estimates of  $q_s$  itself will be agnostic to such variations.

### 315 3.5 Outstanding Challenges

316 Although the GHF modelling framework presented herein provides a powerful method  
 317 to infer GHF from seismological data, a number of outstanding challenges remain. Chief  
 318 amongst them is our inability to reliably infer temperature structure from  $V_S$  at depths  
 319 shallower than the Mohorovičić discontinuity. We have mitigated this issue in three ways:  
 320 by assuming a temperature of 0 °C at the crystalline basement, excising anomalous seis-  
 321 mic data associated with crustal bleeding, and fitting seismically inferred geotherms us-  
 322 ing thermodynamically self-consistent models of shallow thermal structure. However, given  
 323 improved constraints on crustal temperature structure (at vertical resolution of  $\sim 25$  km  
 324 or higher), it would be possible to generate more reliable predictions of surface geother-  
 325 mal gradient. Such constraints may also help in resolving relative contributions to GHF  
 326 derived from transient-state geotherms versus crustal heat production. Pn-waves are a  
 327 type of compressional wave guided along the mantle lid, providing sensitivity to Moho  
 328 temperature structure. Therefore, a high resolution, continental scale model of Antarc-  
 329 tic Pn-velocity ( $V_{Pn}$ ) would be extremely valuable. Fortunately, this may be on the hori-  
 330 zon, with the recent development of a  $V_{Pn}$  model of central West Antarctica (Lucas et  
 331 al., 2021).

332 Secondly, we rely on a parameterisation of geochemical data pertaining to the  
 333 relationship between  $k_0$  and  $V_P$  in order to estimate lateral variations in crustal thermal  
 334 conductivity (Jennings et al., 2019). This parameterisation inherently assumes that con-  
 335 ductivity is sensitive only to silicate content. Further, it assumes that synthetic  $V_P$  es-  
 336 timates from thermodynamic calculations on a range of mineral assemblages are accu-  
 337 rate, and match up to velocities predicted from real data (Behn & Kelemen, 2003). In  
 338 reality, systematic errors in modelled  $V_P$  associated with the choice of regularisation or  
 339 starting model will be propagated into systematic errors in predicted  $k_0$ . In addition,  
 340 artefacts in  $V_P$  structure caused by data sparsity and the ill-posed nature of the seismic  
 341 inversion problem may cause us to improperly estimate  $k_0$  at certain locations. There-  
 342 fore, further validation of methods used to estimate  $k_0(V_P)$  are needed.

343 Finally, the relative sparsity of borehole-derived inferences of Antarctic GHF presents  
 344 a clear challenge in assessing the quality of geophysical predictions. A significant expansion  
 345 of this data set is needed to address the question: what is the most reliable geophys-  
 346 ical method for estimating continental GHF? In addition, multiple boreholes at each field  
 347 sampling region are needed, in order to properly account for localised variations in GHF  
 348 associated with geology, hydrothermal circulation, and topography (Burton-Johnson et  
 349 al., 2020). Promisingly, the Rapid Access Ice Drill (RAID) project seeks to address the  
 350 lack of local data by drilling down to the deepest portions of the Antarctic Ice Sheet (Godge  
 351 & Severinghaus, 2016).

## 352 4 Conclusions

353 We have presented a novel modelling framework for estimating GHF directly from  
 354 seismological data, incorporating lateral variations in crustal composition. We find that  
 355 our geophysical inferences of heat supply are in better agreement with borehole-derived  
 356 estimates than previous studies, implying that crustal conductivity and heat production  
 357 act as significant controls on Antarctic heat flow. Our models of Antarctic conductiv-  
 358 ity, heat production, and GHF provide improved constraints on Antarctic sub-glacial ge-  
 359 ology and thermal conditions, critical for use in ice-sheet modelling studies.

## 360 5 Open Research

361 Figures were prepared using Generic Mapping Tools software. Code and model out-  
 362 puts are provided in an [OSF online repository](#).

## 363 Acknowledgments

364 JANH acknowledges support from the Natural Environment Research Council (Grant  
 365 NE/S007415/1). FDR acknowledges support from the Imperial College Research Fel-  
 366 lowship Scheme. The authors declare no conflicts of interest relevant to this study.

## 367 References

- 368 An, M., Wiens, D. A., Zhao, Y., Feng, M., Nyblade, A., Kanao, M., ... L ev eque,  
 369 J.-J. (2015, December). Temperature, lithosphere-asthenosphere boundary, and  
 370 heat flux beneath the antarctic plate inferred from seismic velocities. *J. Geophys.*  
 371 *Res. Solid Earth*, *120*(12), 8720–8742. doi: 10.1002/2015JB011917
- 372 Artemieva, I. M., Thybo, H., Jakobsen, K., S orensen, N. K., & Nielsen, L. S. K.  
 373 (2017). Heat production in granitic rocks: Global analysis based on a new  
 374 data compilation granite2017. *Earth-Science Reviews*, *172*, 1–26. doi:  
 375 10.1016/j.earscirev.2017.07.003
- 376 Ball, P. W., White, N. J., MacLennan, J., & Stephenson, S. N. (2021). Global in-  
 377 fluence of mantle temperature and plate thickness on intraplate volcanism. *Nature*

- 378 *Communications*, 12(1), 2045. doi: 10.1038/s41467-021-22323-9
- 379 Barletta, V. R., Bevis, M., Smith, B. E., Wilson, T., Brown, A., Bordoni, A., ...  
 380 Wiens, D. A. (2018). Observed rapid bedrock uplift in amundsen sea em-  
 381 bayment promotes ice-sheet stability. *Science*, 360(6395), 1335–1339. doi:  
 382 10.1126/science.aao1447
- 383 Behn, M. D., & Kelemen, P. B. (2003). Relationship between seismic p-wave  
 384 velocity and the composition of anhydrous igneous and meta-igneous rocks.  
 385 *Geochemistry, Geophysics, Geosystems*, 4(5). doi: [https://doi.org/10.1029/  
 386 2002GC000393](https://doi.org/10.1029/2002GC000393)
- 387 Burton-Johnson, A., Dziadek, R., & Martin, C. (2020). Review article: Geothermal  
 388 heat flow in antarctica: current and future directions. *The Cryosphere*, 14(11),  
 389 3843–3873. doi: 10.5194/tc-14-3843-2020
- 390 Faul, U. H., & Jackson, I. (2005). The seismological signature of temperature and  
 391 grain size variations in the upper mantle. *Earth and Planetary Science Letters*,  
 392 234(1), 119–134. doi: 10.1016/j.epsl.2005.02.008
- 393 Faul, U. H., Jackson, I., & X, Y. (2007, April). Diffusion creep of dry, melt-free  
 394 olivine. *J. Geophys. Res.*, 112(B4). doi: 10.1029/2006JB004586
- 395 Goes, S., Hasterok, D., Schutt, D. L., & Klöcking, M. (2020). Continental litho-  
 396 spheric temperatures: A review. *Physics of the Earth and Planetary Interiors*,  
 397 306, 106509. doi: 10.1016/j.pepi.2020.106509
- 398 Goodge, J. W., & Severinghaus, J. P. (2016). Rapid access ice drill: a new tool  
 399 for exploration of the deep antarctic ice sheets and subglacial geology. *Journal of  
 400 Glaciology*, 62(236), 1049–1064. doi: 10.1017/jog.2016.97
- 401 Haeger, C., Petrunin, A. G., & Kaban, M. K. (2022). Geothermal heat flow and  
 402 thermal structure of the antarctic lithosphere. *Geochemistry, Geophysics, Geosys-  
 403 tems*, 23(10), e2022GC010501. (e2022GC010501 2022GC010501) doi: [https://doi  
 404 .org/10.1029/2022GC010501](https://doi.org/10.1029/2022GC010501)
- 405 Hasterok, D., & Chapman, D. S. (2011). Heat production and geotherms for the  
 406 continental lithosphere. *Earth and Planetary Science Letters*, 307(1), 59–70. doi:  
 407 10.1016/j.epsl.2011.04.034
- 408 Hazzard, J. A. N., Richards, F. D., Goes, S. D. B., & Roberts, G. G. (2023). Prob-  
 409 abilistic assessment of antarctic thermomechanical structure: Impacts on ice sheet  
 410 stability. *Journal of Geophysical Research: Solid Earth*, 128(5), e2023JB026653.  
 411 doi: 10.1029/2023JB026653
- 412 Jennings, S., Hasterok, D., & Payne, J. (2019, August). A new compositionally  
 413 based thermal conductivity model for plutonic rocks. *Geophysical Journal Interna-  
 414 tional*, 219(2), 1377–1394. doi: 10.1093/gji/ggz376
- 415 Korenaga, T., & Korenaga, J. (2016). Evolution of young oceanic lithosphere and  
 416 the meaning of seafloor subsidence rate. *Journal of Geophysical Research: Solid  
 417 Earth*, 121(9), 6315–6332. doi: <https://doi.org/10.1002/2016JB013395>
- 418 Larour, E., Morlighem, M., Seroussi, H., Schiermeier, J., & Rignot, E. (2012). Ice  
 419 flow sensitivity to geothermal heat flux of pine island glacier, antarctica. *Journal  
 420 of Geophysical Research: Earth Surface*, 117(F4). doi: [https://doi.org/10.1029/  
 421 2012JF002371](https://doi.org/10.1029/2012JF002371)
- 422 LeMasurier, W. E. (2008). Neogene extension and basin deepening in the west  
 423 antarctic rift inferred from comparisons with the east african rift and other  
 424 analogs. *Geology*, 36(3), 247–250.
- 425 Lloyd, A. J., Wiens, D. A., Zhu, H., Tromp, J., Nyblade, A. A., Aster, R. C., ...  
 426 O'Donnell, J. P. (2020). Seismic structure of the antarctic upper mantle imaged  
 427 with adjoint tomography. *Journal of Geophysical Research: Solid Earth*, 125(3).  
 428 doi: 10.1029/2019JB017823
- 429 Lucas, E. M., Nyblade, A. A., Lloyd, A. J., Aster, R. C., Wiens, D. A., O'Donnell,  
 430 J. P., ... Huerta, A. D. (2021). Seismicity and pn velocity structure of central  
 431 west antarctica. *Geochemistry, Geophysics, Geosystems*, 22(2), e2020GC009471.

- (e2020GC009471 2020GC009471) doi: <https://doi.org/10.1029/2020GC009471>
- 432  
433 Lucazeau, F. (2019). Analysis and mapping of an updated terrestrial heat flow data  
434 set. *Geochemistry, Geophysics, Geosystems*, *20*(8), 4001–4024. doi: [https://doi](https://doi.org/10.1029/2019GC008389)  
435 [.org/10.1029/2019GC008389](https://doi.org/10.1029/2019GC008389)
- 436 Lösing, M., Ebbing, J., & Szwillus, W. (2020). Geothermal heat flux in antarctica:  
437 Assessing models and observations by bayesian inversion. *Frontiers in Earth Sci-*  
438 *ence*, *8*. doi: 10.3389/feart.2020.00105
- 439 Martos, Y. M., Catalán, M., Jordan, T. A., Golynsky, A., Golynsky, D., Eagles, G.,  
440 & Vaughan, D. G. (2017). Heat flux distribution of antarctica unveiled. *Geo-*  
441 *physical Research Letters*, *44*(22), 11,417–11,426. doi: [https://doi.org/10.1002/](https://doi.org/10.1002/2017GL075609)  
442 [2017GL075609](https://doi.org/10.1002/2017GL075609)
- 443 McCarthy, C., & Takei, Y. (2011, September). Anelasticity and viscosity of partially  
444 molten rock analogue: Toward seismic detection of small quantities of melt. *Geo-*  
445 *phys. Res. Lett.*, *38*(18). doi: 10.1029/2011GL048776
- 446 McKenzie, D., Jackson, J., & Priestley, K. (2005). Thermal structure of oceanic and  
447 continental lithosphere. *Earth and Planetary Science Letters*, *233*(3), 337–349.  
448 doi: <https://doi.org/10.1016/j.epsl.2005.02.005>
- 449 Press, W. H., Teukolsky, S. A., Vetterling, W. T., & Flannery, B. P. (2007). *Numeri-*  
450 *cal recipes: The art of scientific computing* (Third edition ed.). Cambridge Univer-  
451 sity Press.
- 452 Richards, F. D., Hoggard, M. J., White, N., & Ghelichkhan, S. (2020). Quantifying  
453 the relationship between short-wavelength dynamic topography and thermome-  
454 chanical structure of the upper mantle using calibrated parameterization of anelas-  
455 ticity. *Journal of Geophysical Research: Solid Earth*, *125*(9), e2019JB019062. doi:  
456 [10.1029/2019JB019062](https://doi.org/10.1029/2019JB019062)
- 457 Sammon, L. G., McDonough, W. F., & Mooney, W. D. (2022). Compositional at-  
458 tributes of the deep continental crust inferred from geochemical and geophysical  
459 data. *Journal of Geophysical Research: Solid Earth*, *127*(8), e2022JB024041.  
460 (e2022JB024041 2022JB024041) doi: <https://doi.org/10.1029/2022JB024041>
- 461 Sauli, C., Sorlien, C., Busetti, M., De Santis, L., Geletti, R., Wardell, N., &  
462 Luyendyk, B. (2021). Neogene development of the terror rift, western ross sea,  
463 antarctica. *Geochemistry, Geophysics, Geosystems*, *22*(3), e2020GC009076.
- 464 Shen, W., Wiens, D. A., Lloyd, A. J., & Nyblade, A. A. (2020). A geothermal heat  
465 flux map of antarctica empirically constrained by seismic structure. *Geophysical*  
466 *Research Letters*, *47*(14), e2020GL086955. (e2020GL086955 2020GL086955) doi:  
467 <https://doi.org/10.1029/2020GL086955>
- 468 Twinn, G., Riley, T., Fox, M., & Carter, A. (2022). Thermal history of the south-  
469 ern antarctic peninsula during cenozoic oblique subduction. *Journal of the Geolog-*  
470 *ical Society*, *179*(6), jgs2022–008.
- 471 Yabe, K., & Hiraga, T. (2020). Grain-boundary diffusion creep of olivine: 2. solidus  
472 effects and consequences for the viscosity of the oceanic upper mantle. *Journal of*  
473 *Geophysical Research: Solid Earth*, *125*(8). doi: 10.1029/2020JB019416
- 474 Yamauchi, H., & Takei, Y. (2016). Polycrystal anelasticity at near-solidus tempera-  
475 tures. *Journal of Geophysical Research: Solid Earth*, *121*(11), 7790–7820. doi: 10  
476 [.1002/2016JB013316](https://doi.org/10.1002/2016JB013316)
- 477 Zwally, H. J., & Giovinetto, M. B. (2011). Overview and assessment of antarctic ice-  
478 sheet mass balance estimates: 1992–2009. *Surveys in Geophysics*, *32*(4), 351–376.  
479 doi: 10.1007/s10712-011-9123-5